Hypohydrostatic Simulation of a Quasi-Steady Baroclinic Cyclone

TSUNG-LIN HSIEH

Program in Atmospheric and Oceanic Sciences, Princeton University, Princeton, New Jersey

STEPHEN T. GARNER

NOAA/Geophysical Fluid Dynamics Laboratory, Princeton, New Jersey

ISAAC M. HELD

Program in Atmospheric and Oceanic Sciences, Princeton University, Princeton, New Jersey

(Manuscript received 25 October 2019, in final form 24 January 2020)

ABSTRACT

Simulations of baroclinic cyclones often cannot resolve moist convection but resort to convective parameterization. An exception is the hypohydrostatic rescaling, which in principle can be used to better represent convection with no increase in computational cost. The rescaling is studied in the context of a quasi-steady, convectively active, baroclinic cyclone. This is a novel framework with advantages due to the unambiguous time-mean structure. The rescaling is evaluated against high-resolution solutions up to a 5-km grid spacing. A theoretical scaling combining convective-scale dynamics and synoptic-scale energy balance is derived and verified by the simulations. It predicts the insensitivity of the large-scale flow to resolution finer than 40 km and to moderate rescaling, and a weak bias in the cyclone intensity under very large rescaling. The theory yields a threshold for the rescaling factor that avoids large-scale biases. Below the threshold, the rescaling can be used to control resolution errors at the convective scale, such as the distribution of extreme precipitation rates.

1. Introduction

The hypohydrostatic rescaling is a computational trick that has gained some popularity in modeling studies of the interaction of moist convection with large-scale flows. Its definition is as simple as attaching a constant nondimensional parameter α to the vertical acceleration term:

$$\alpha^2 \frac{dw}{dt} = -\frac{1}{\rho}\partial_z p - g. \qquad (1)$$

The physical equation is recovered with $\alpha = 1$; while $\alpha = 0$ gives the hydrostatic approximation. With $\alpha > 1$, the equation becomes more nonhydrostatic than the original, and hence is referred to as "hypohydrostatic."

The rescaling directly alters nonhydrostatic convection by decreasing its vertical velocity and increasing its width, as observed in cloud-permitting, radiative–convective equilibrium (RCE) simulations (Pauluis et al. 2006; Boos et al. 2016) with $\alpha = O(10)$ and a grid scale of $\Delta x \approx 10$ km. In coarse resolution, global aquaplanet simulations (Garner et al. 2007; Semane and Bechtold 2015), larger values of $\alpha = O(100)$ are required to widen the convection beyond the grid scale of $\Delta x \approx 100$ km. The rescaling may be considered as a replacement for convective parameterization in the sense that convection is resolved by a smaller effective grid spacing $\Delta x_{\mathrm{eff}} \equiv \Delta x/\alpha$ (Kuang et al. 2005; Pauluis et al. 2006), to the extent that it is not influenced by the planetary radius or rotation.

The rescaling has several benefits compared with conventional parameterization schemes. First, unlike parameterization schemes that target a specific phenomenon, the rescaling applies simultaneously to deep convection, shallow convection, and nonhydrostatic gravity waves. Therefore, it does not need to be redesigned from a GCM to a cloud-resolving model. Second, all subgrid processes, including moist static energy flux and momentum flux, are consistently modified.

Denotes content that is immediately available upon publication as open access.

Corresponding author: Tsung-Lin Hsieh, hsiehtl@princeton.edu

DOI: 10.1175/JAS-D-19-0300.1

Third, with only one tuning parameter, α, it is simple to optimize. Last, it requires no additional computational cost to the original model, and avoids the technical complication of interfacing the dynamical core with a separate routine.

Because of those benefits, the hypohydrostatic rescaling has been applied to study the South Asian monsoon (Ma et al. 2014, 2019), tropical cyclones (Fedorov et al. 2018), the Hadley circulation (Singh and Kuang 2016; Singh et al. 2017), low-frequency tropical variabilities (Peters and Bretherton 2006; Boos and Kuang 2010), and climate sensitivity (Bretherton 2007).

Despite its apparent simplicity, how the rescaling influences the large-scale flow is not straightforward and depends on the particular phenomenon. Sensitivity tests on α and comparison against high-resolution solutions have been performed in RCE with background shear (Pauluis et al. 2006), self-aggregating RCE without background shear, and rotating RCE states (Boos et al. 2016). In Pauluis et al. (2006), where convective self-aggregation does not occur, the rescaling worsened resolution errors in several moisture fields, creating a dry bias in the free troposphere, for example. They attributed the bias to the slowdown of shallow convection, which reduces the moisture transport from the boundary layer to the free troposphere.

On the other hand, Boos et al. (2016) reported some positive results with the rescaling. Several resolution biases associated with the aggregated convection were corrected, possibly due to the slowdown of gravity waves. In their rotating RCE experiments, the maximum intensity of tropical cyclones is increased by the rescaling and becomes closer to the high-resolution solution. Those examples show that the hypohydrostatic rescaling has both desirable and undesirable consequences, but no rule exists, a priori, for whether the former outweighs the latter.

In this study, we quantify how the rescaling influences the model of a baroclinic eddy, in order to bound the values of α that avoid undesirable biases. The baroclinic eddy is an interesting phenomenon wherein both convective instability and baroclinic instability act to stabilize the atmosphere. The convection–eddy interaction has been difficult to study, though, because of the significant computational cost to simultaneously resolve convection and the eddy. As high-resolution global models ($\Delta x \approx 25\,\mathrm{km}$) become more common, moisture transport by the explicit convection becomes comparable to the parameterized transport and has nontrivial influence on the eddy intensity (Boutle et al. 2011; Booth et al. 2017). Resolution experiments of Willison et al. (2013) and Booth et al. (2013) up to a 20-km horizontal grid spacing showed that better resolved convective systems increase the eddy intensity.

To focus on simulating the convection–eddy interaction, we adopt a classic model configuration for baroclinic life cycle simulations. The domain is a zonally periodic channel, in which the zonal dimension is limited to a sector to reduce the computational cost. At the expense of representing long waves, it is then easier to run the model at cloud-permitting resolutions without parameterized convection, which is necessary for a direct examination of the rescaling effect.

Studies using such a channel model have usually focused on the transient growth of the cyclone. The mature cyclone that develops in this process may persist for several days (e.g., Thorncroft et al. 1993) but has received much less attention in the literature than the full life cycle. Here, we introduce external forcing and dissipation to further extend the lifetime of the mature cyclone. For reasons that are not fully understood, the baroclinic eddy becomes quasi steady after developing from a weak disturbance, with a consistent phase speed and no pronounced amplitude variability. While we have not fully explored the necessary and sufficient conditions for this behavior, it is consistent with the longevity of baroclinic cyclones in Thorncroft et al. (1993) and Orlanski (2003). The steadiness facilitates our analysis, as robust statistics can be measured.

The goal of this paper is, first, to identify resolution biases of simulating a moist baroclinic eddy at a typical GCM resolution, and then to examine the impact of the hypohydrostatic rescaling on the biases. The work is complementary to previous evaluation studies of Pauluis et al. (2006) and Boos et al. (2016) that focused on RCE states. At the finest resolution, the present experiments are much better resolved than previous idealized studies of equilibrated baroclinic eddies.

2. Model configuration

The hypohydrostatic rescaling, Eq. (1), is implemented in a nonhydrostatic, fully compressible dynamical core, ZETAC, described in Pauluis et al. (2006) and Garner et al. (2007). Strategies for implementing this rescaling in models having relatively straightforward vertical advection schemes are described in Kuang et al. (2005) and Pauluis et al. (2006). Equivalent implementation in a spectral model is described in Semane and Bechtold (2015). This model has also been used in several studies of tropical cyclones in the North Atlantic (Knutson et al. 2007, 2013) and North Pacific (Wu et al. 2014). The β-plane, Cartesian channel is zonally periodic with a reference Coriolis parameter at 40°N. The domain spans 5600 km in latitude and 4080 km in longitude, corresponding to a meridional range between 15° and 65°N. The northern and southern boundaries are sponges of thickness 5° in latitude, in which the horizontal velocities are nudged to zero but other fields are unaltered. The model has 45 vertical levels, with resolution increasing from 45 m near the surface to 654 m above 4 km. Between 12 and 20 km is an upper sponge layer where the potential temperature is nudged to a typical stratospheric profile.

The prescribed SST is zonally uniform with an idealized meridional structure. Specifically, the SST is 304 K between 15° and 35°N, transitions smoothly to 277 K at 55°N, and stays constant to the northern boundary. The surface fluxes are parameterized using the bulk aerodynamic formula with surface winds from the Monin–Obukhov similarity theory and a constant roughness length. The moist boundary layer scheme, following Grenier and Bretherton (2001), and the radiative transfer scheme are taken from the AM2.1 model (Anderson et al. 2004) developed at the Geophysical Fluid Dynamics Laboratory. The solar zenith angle is fixed at 40°N with no diurnal cycle. All radiative gases are active, but the cloud radiative forcing is turned off as we aim to study the dynamical, not radiative, influence of the expanded convection. The microphysics is a six-species, single-moment scheme following Krueger et al. (1995). No shallow or deep cumulus parameterization is used, because the uncertainty of applying the same parameterization to different cloud-permitting resolutions would complicate the analysis. When the horizontal resolution is changed, the ∇^4 hyperdiffusivity is scaled with $(\Delta x)^4$ to preserve the diffusion time scale for a $2\Delta x$ wave.

For the resolution study, four simulations without the hypohydrostatic rescaling are performed at $\Delta x = \Delta y =$ 40, 20, 10, and 5 km. The rescaling study consists of simulations at $\Delta x = \Delta y = 40$ km with $\alpha = 1, 2, 4, 8, 16, 32,$ 40, 60, 80, 100, and 200. The computational cost increases with $(\Delta x)^{-3}$ in the resolution experiments because of the increased resolutions in x, y, t; while the cost is unchanged in the rescaling experiments. The vertical resolution is the same in all simulations.

3. Characteristics of the quasi-steady baroclinic eddy

In this model, the initial disturbance evolves into a baroclinic eddy that stays quasi steady in time. Its characteristics are presented in this section, and its relevance to a realistic mature baroclinic eddy is discussed. This section focuses on the synoptic-scale structures of the unscaled ($\alpha = 1$) solutions that are insensitive to horizontal resolution.

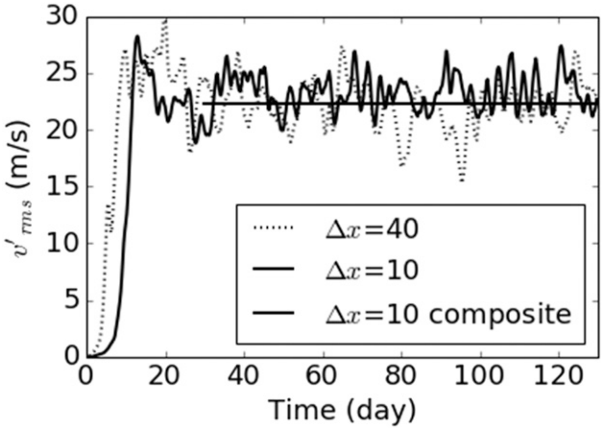

FIG. 1. Time series of eddy intensity, measured by the mass-weighted root-mean-square of v', showing the steadiness of the final state. The composite eddy is averaged over time from day 30 onward.

With the eightfold periodicity in the zonal direction, a wavenumber-1 baroclinic cyclone develops in the model as a wavenumber-8 global perturbation. An initial sinusoidal perturbation is superposed on a zonally symmetric initial state in thermal wind balance. The time series of eddy amplitude at $\Delta x = 40$ and 10 km are shown in Fig. 1. Simulations at other resolutions are initialized from the equilibrated $\Delta x = 40$-km solution. In all simulations performed, the eddies become quasi steady at finite amplitude, typically after 2 weeks. All time averages in this study are taken from day 30 onward.

The left column of Fig. 2 shows typical snapshots of the precipitation rate in the statistically steady state, overlaid with contours of boundary layer temperature. The cyclone is manifested as the comma cloud plus the frontal squall line. The latter is indicated by a line of deep convection at the western boundary of the warm sector. The cyclone travels eastward with a constant phase speed.

In the tropics, the warm SST sets off active tropical cyclogenesis. The tropical cyclones (TCs) migrate into the warm sector of the baroclinic cyclone, where they are destroyed by the wind shear. This process gives rise to most of the temporal variability in the time series (Fig. 1). The sizes and shapes of the convective systems are affected by the grid. For instance, TCs in low-resolution simulations are usually oversized, as seen in the snapshots.

Small-scale variations can be filtered out by compositing the snapshots in the reference frame of the baroclinic wave, which is tracked by locating the surface pressure maximum between 45° and 60°N. The intensity of the resulting composite eddy, measured by the root-mean-square v', captures over 95% of the root-mean-square v'

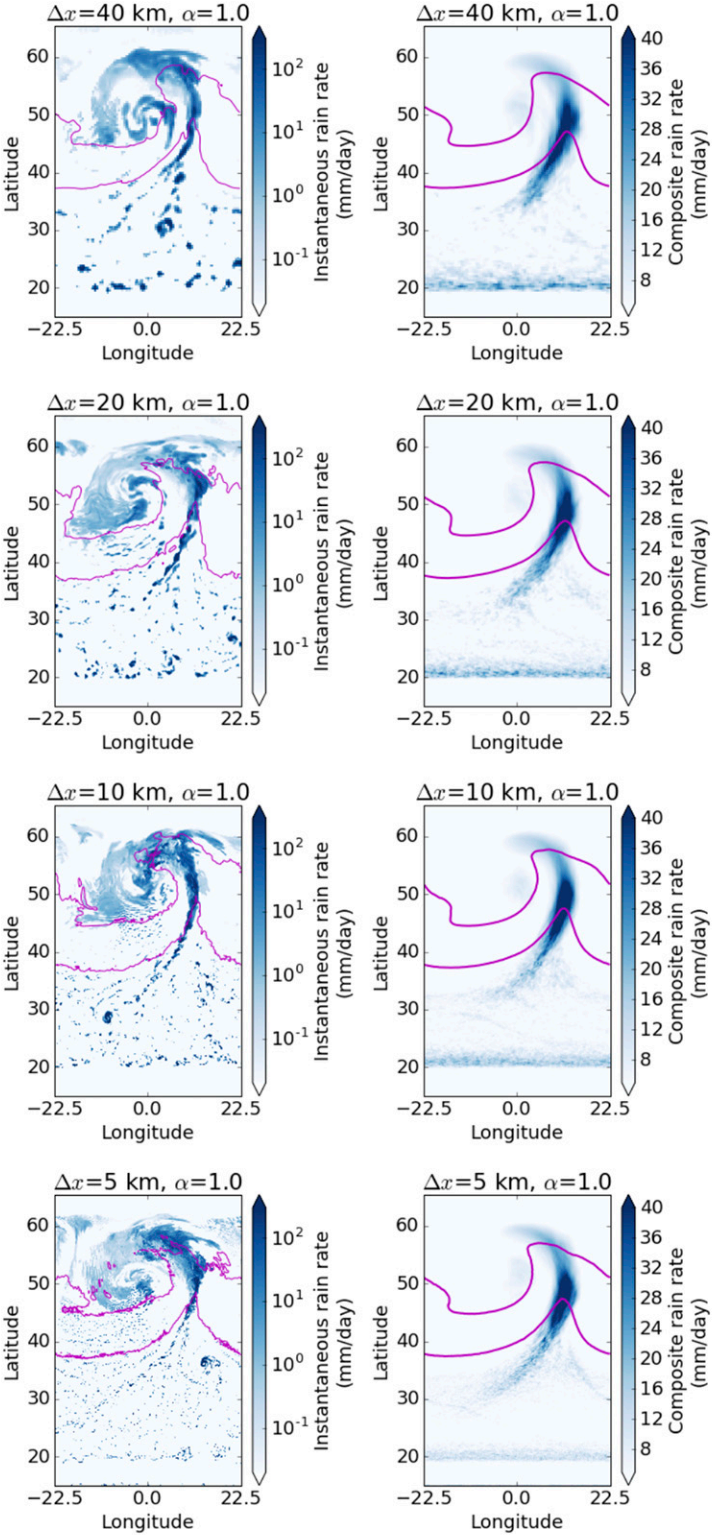

FIG. 2. (left) Instantaneous rain rate overlaid with 280- and 290-K temperature contours at $z = 1$ km at different horizontal resolutions. (right) Composites of the same fields. Note the that the color scale is logarithmic in the snapshots and linear in the composites, but is consistent across resolutions. The absolute value of longitude is arbitrary in this aquaplanet model, but the range of 45° indicates the eightfold periodicity.

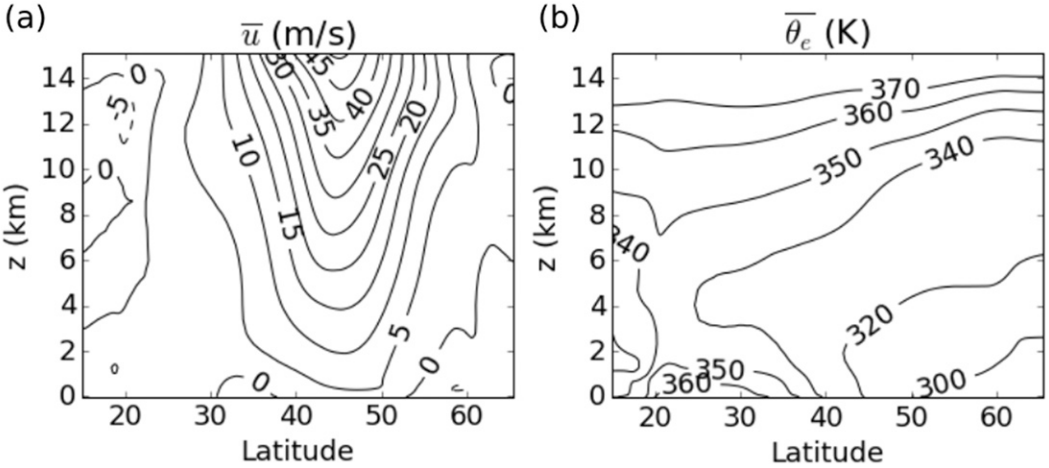

FIG. 3. Zonal, temporal mean (a) zonal wind (b) equivalent potential temperature in the quasi-steady state for $\Delta x = 10$ km, $\alpha = 1$.

over time (Fig. 1). The right column of Fig. 2 shows composites of the same fields as in the left column. The general structures of rain and temperature are very similar to the snapshots, a consequence of the steady large-scale flow. The reduced peak precipitation and the widened spatial spread of the composite frontal squall line reflect the spatial–temporal intermittency of convection.

In the low latitudes, a narrow rainband analogous to the ITCZ can be observed near the boundary of the sponge layer at 20°N. The ITCZ occurs because the sponge at the south damps the horizontal velocity, which is mostly associated with convective activity. Thus, mean ascent at the ITCZ and subsidence at the sponge form an overturning circulation. Together with another branch extending from the ITCZ to 30°N, the overturning circulation in the low latitudes is analogous to the Hadley circulation.

In the zonal and temporal mean, a westerly jet having realistic strength (Fig. 3a) forms to the south of the eddy, similar to the LC2 pattern in Thorncroft et al. (1993). Latitudes to the south of 25°N resemble the tropics, with little vertical wind shear and nearly moist neutral stratification (Fig. 3b). The transition zone between 25° and 35°N serves as the subtropics, where sporadic convection occurs within an environment dominated by large-scale subsidence. This is a desirable self-contained hemispheric system: given a fairly warm SST in the low latitudes, it is possible to maintain realistic upper-tropospheric baroclinicity with a narrow tropics, which frees up the model grid for resolving the midlatitude dynamics.

The vertical structure of the eddy is visualized by the longitude–altitude cross section of composite v and θ_e in Fig. 4. In the lower levels, the poleward flow is roughly in phase with the warm anomaly. A northward low-level jet exists at around 1-km altitude, transporting much of the heat and moisture poleward. The longitude of maximum v tilts westward with height up to 4 km, above which resides an equivalent barotropic eddy in thermal wind balance, where v and θ_e are out of phase in x and have little tilt in z. The flow structure is similar to a typical observed baroclinic cyclone, with a low-level jet locating to the east of the upper-level southerly peak (Lackmann 2002). The warm sector located around 10°E (the absolute longitude is arbitrary in this aquaplanet model) is nearly moist neutral, suggesting the importance of convection in setting the stratification. In the cold sector, the equatorward-moving dry air over the warm ocean leads to strong evaporation and rapid mixing in the boundary layer, topped by shallow clouds with light precipitation, which is visible as the light-blue shading in the snapshots (Fig. 2).

4. Convective-scale-resolution biases corrected by α

Mathematical similarity explains how motions at limiting scales respond to the hypohydrostatic rescaling

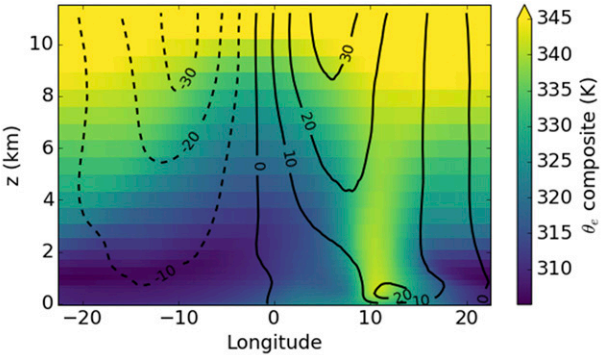

FIG. 4. Cross section on the x–z plane of the composite v (black contours) and θ_e (color shading) for $\Delta x = 10$ km, $\alpha = 1$ at 45°N.

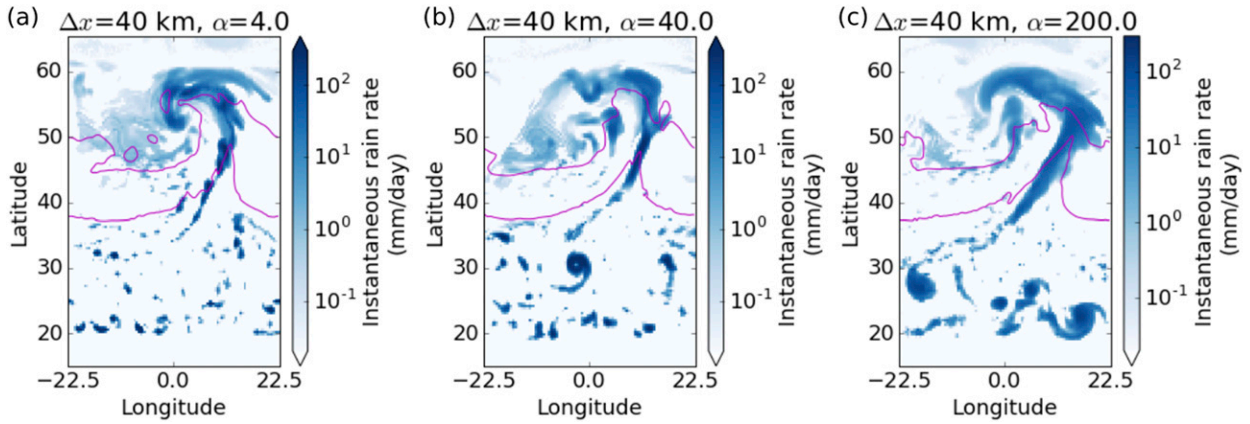

FIG. 5. As in Fig. 2, but for Δx = 40 km and (a) α = 4, (b) α = 40, and (c) α = 200. The expansion of convection is limited in (a) but more apparent in (b) and (c).

(Pauluis et al. 2006; Garner et al. 2007). Purely hydrostatic circulations are transparent to α as the right-hand side of Eq. (1) is exactly balanced. On the other hand, a convective cell, being much smaller than the planetary radius and much quicker than planetary rotation and external forcings, undergoes the following transformation (Pauluis et al. 2006):

$$x_{(\alpha>1)} = \alpha x_{(\alpha=1)}, \tag{2a}$$

$$t_{(\alpha>1)} = \alpha t_{(\alpha=1)}, \tag{2b}$$

$$w_{(\alpha>1)} = w_{(\alpha=1)}/\alpha. \tag{2c}$$

This transformation essentially dilates the coordinate system associated with convection. The similarity involving α and Δx implied by Eq. (2a) means that holding $\Delta x_{\text{eff}} \equiv \Delta x/\alpha$ constant tends to preserve the characteristics of the convection. With respect to the large-scale flow, convection appears wider but the geometric shape is mathematically similar to an ordinary, unscaled convection. However, while the depth of convection remains the same, it has a slower vertical velocity. The similarity arguments apply strictly to the limiting motions, and motions in between those two limits are analyzed in this section. We focus entirely on midlatitude convection to the north of 40°N.

a. *Area of hypohydrostatic convection*

Figure 5 displays snapshots of rain rate and boundary layer temperature (the same fields shown in Fig. 2) from three of the eleven α simulations applied at Δx = 40 km. Because the model grid is not modified, better resolved convection appears as expanded convection. Artifacts due to the shape of grid boxes become less apparent, and the structure of the convective systems is better represented. Despite the differences on the small scale, the large-scale features remain qualitatively similar across the α simulations, with a baroclinic cyclone dominating the midlatitude dynamics.

Figure 6 quantifies the expansion of convective clusters with α, in particular those associated with the baroclinic cyclone, which have not been studied in the literature. A convective cluster is identified as a connected group of grid columns whose instantaneous rain rates are in the top 1% of the distribution. This threshold is approximately 100 mm day^{-1}, but the exact value has little influence on the analysis because of the rapid decrease of rain rate outward from the convective cell boundary. Large rain rates correspond to strong vertical

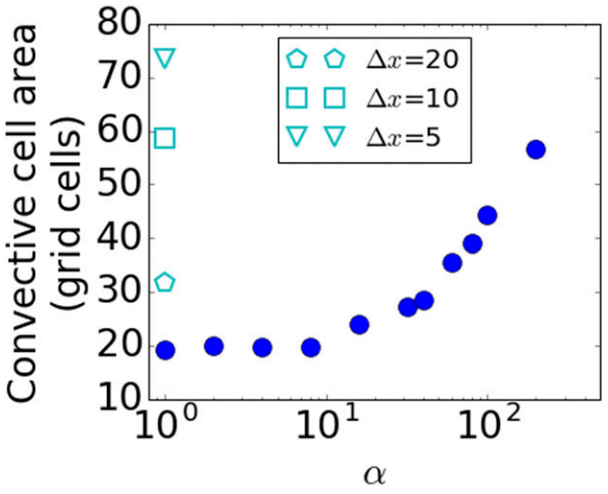

FIG. 6. Average size of convective cells in units of grid columns, showing that convection is better resolved with either decreasing Δx or increasing α. The physical area of convection decreases with decreasing Δx but has not converged.

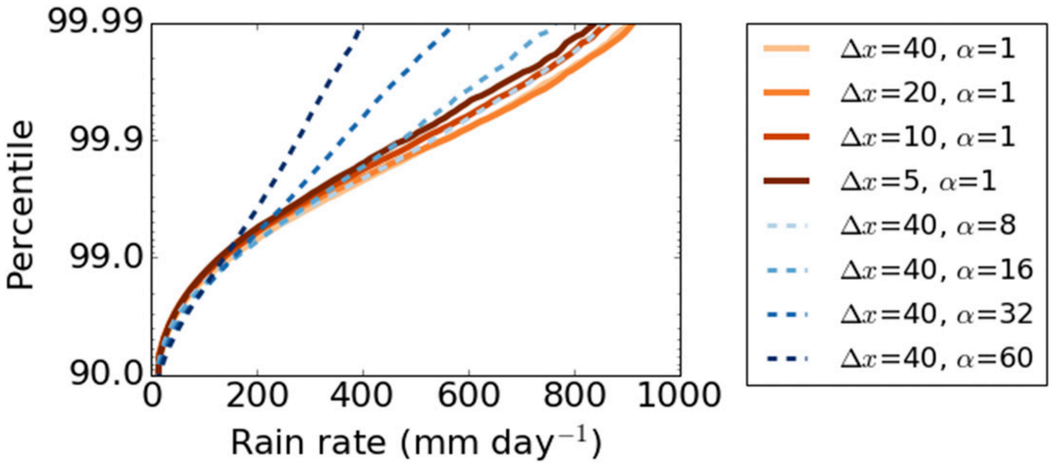

FIG. 7. Distribution of instantaneous rain rate. Note that the vertical axis is in logarithmic scale to emphasize the extreme values. Curves with darker blue better match curves with darker orange, indicating the resolution bias is corrected by the hypohydrostatic rescaling.

moisture fluxes in our model without parameterized precipitation. Note that we do not differentiate convection from the rapidly ascending warm conveyor belt, as they are often indistinguishable (Oertel et al. 2019). This procedure is performed for every 6-hourly snapshot, yielding sample sizes on the order of 10^3 in each simulation.

The circular markers in Fig. 6 show that the average area of convection is about 20 grid cells for $\alpha \lesssim 8$ or $\Delta x_{\mathrm{eff}} = \Delta x/\alpha \gtrsim 5$ km, corresponding to a width of $5\Delta x$. This insignificant expansion suggests that convection is not resolved by $\Delta x_{\mathrm{eff}} \gtrsim 5$ km, so convective instability at the grid scale remains dominant. On the other hand, $\alpha \gtrsim 8$ leads to monotonic expansion of convection until at least $\alpha = 200$ or $\Delta x_{\mathrm{eff}} = 0.2$ km, confirming the expectation that the hypohydrostatic rescaling helps resolve convection. As a reference, the resolution study of squall-line convection by Lebo and Morrison (2015) suggested that it requires $\Delta x \lesssim 0.25$ km for the average cloud area to converge.

The polygonal markers in Fig. 6 show the average area of convection in high-resolution simulations (throughout the paper, the figures use the convention that markers with fewer faces represent smaller grid spacings). The area is expressed in terms of number of grid cells, with better-resolved convection covering more grid cells. Comparing across the $\alpha = 1$ resolution experiments, the area increases by less than a factor of 4 when the grid spacing is halved, because the area is still somewhat quantized by the grid.

The rescaling and resolution experiments with the same Δx_{eff} do not have the same average convection area, because large, hydrostatic convection does not follow the grid-based similarity based on Eq. (2a). For instance, the average area with $\Delta x = 40$ km, $\alpha = 8$ is smaller than that with $\Delta x = 5$ km, $\alpha = 1$. This is because large convection in the rescaled solution will have large physical area, but there may not be enough room within the large-scale convecting region. This analysis shows that even though increasing α better resolves convection in the way decreasing Δx does, the dependence is not straightforward due to the finite grid spacing and large-scale inhomogeneity.

b. *Distribution of extreme rain rate*

Extreme rain rates for the resolution and rescaling experiments are given in Fig. 7, which shows a resolution error that can be controlled by α. The distribution is constructed using every grid point in the domain in the 6-hourly snapshots and expressed in terms of percentile values. To establish a fair comparison across different grids, the high-resolution data are coarse grained to the 40-km grid. In the fully resolved limit, the distribution of the coarse-grained data should not change with its native resolution.

The different shades of orange curves in Fig. 7 show that extreme rain rates occur too frequently in the 40-km solution, as the 40-km curve is everywhere to the right of the higher-resolution curves for large rain rates. Physically, it means that when the 40 km × 40 km grid cell is convecting, it produces an unrealistically large rain rate averaged over this area. The reason may be understood from the following example. The area of an isolated convective cell increases by a factor of 4 when the grid spacing is doubled (resolution is decreased), assuming the width of convection is limited to a fixed number of grid points. Its vertical velocity is decreased by

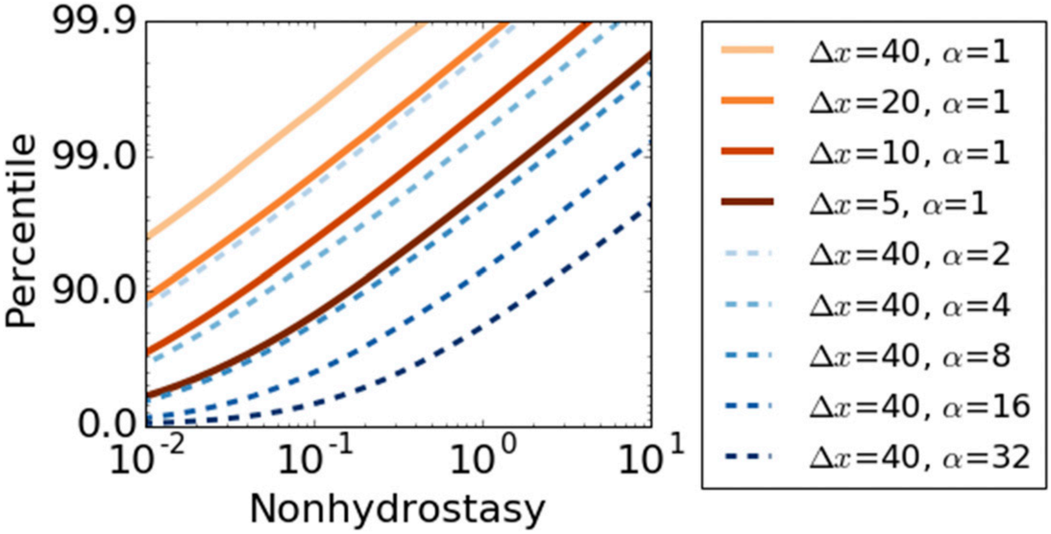

FIG. 8. Distribution of the nonhydrostasy, $|\partial_x[\alpha^2(dw/dt)]/(\partial_x\theta/\theta)g|$, which is larger when the grid cell is more nonhydrostatic. That the distribution shifts toward the right with increasing resolution (darker orange) or increasing rescaling (darker blue) suggests that nonhydrostatic effects are better represented.

only a factor of 2 in the hydrostatic limit, and it does not decrease in the fully nonhydrostatic limit. In either limit, precipitation by an isolated convective cell increases with grid spacing when averaged over a coarse-grained area. In practice, the high-resolution solution may have multiple convective cells in a coarse-grained area, but the leftward shift of the orange curves with increasing resolution in Fig. 7 suggests that the cloud fraction does not increase enough to compensate for the area-mean decrease.

The overestimation of extreme rain rates in the 40-km model may be controlled by α. As shown by the blue dashed curves in Fig. 7, extreme rain rates are reduced with increasing α as the vertical velocity decreases, making the distributions more similar to those of high resolutions. Note that it is not expected that the large α distributions will match the high-resolution distributions, because the similarity argument applies only locally around a single convective cell (discussed further in section 5a). Despite the changing extreme rain rates, the mean rain rate is insensitive to resolution or to moderate rescaling (discussed further in section 5c).

c. *Distribution of nonhydrostasy*

A principal purpose of applying the hypohydrostatic rescaling is to enhance nonhydrostatic effects, which are underestimated at $\Delta x = 40$ km. The nonhydrostasy reflects the relative importance of the inertial term in the vertical momentum equation [Eq. (1)]. Figure 8 shows distributions of the ratio

$$\left|\partial_x\left(\alpha^2\frac{dw}{dt}\right)\Big/\frac{\partial_x\theta}{\theta}g\right| \qquad (3)$$

at every grid cell in the domain at $z = 6$ km. The ratio is an approximation of $\partial_x\beta/\partial_x B$, where $\beta = \alpha^2 dw/dt$ is the effective buoyancy and B is the Archimedean buoyancy. These two buoyancies will be discussed further in section 5 and are important for predicting the vertical velocity. The nonhydrostasy is sometimes measured by β/B (e.g., Jeevanjee 2017). Here the x derivatives are applied to filter out the background buoyancy that is balanced by hydrostatic pressure, retaining the dynamically relevant nonhydrostatic buoyancy to better probe the small scales.

A smaller ratio corresponds to a more hydrostatic grid cell. For instance, a ratio smaller than 10^{-1} indicates that the hydrostatic balance is accurate to within 10%. This regime is on the left side of Fig. 8. For $\Delta x = 40$ km and $\alpha = 1$, the 10^{-1} ratio is above the 99th percentile, meaning that over 99% of the domain is approximately hydrostatic. This percentage is dropped to 85% at $\Delta x = 5$ km but has not converged with resolution, so it is expected to be even smaller in a fully resolved solution. That is, the 40-km solution significantly underestimates the area where nonhydrostatic effects occur. With increasing α, the distributions in Fig. 8 shifts toward the right, meaning that more grid cells become nonhydrostatic. The hypohydrostatic rescaling makes the system more nonhydrostatic as does increasing resolution.

5. Synoptic-scale biases due to large α

Despite better resolving convection and better representing nonhydrostatic effects, the hypohydrostatic

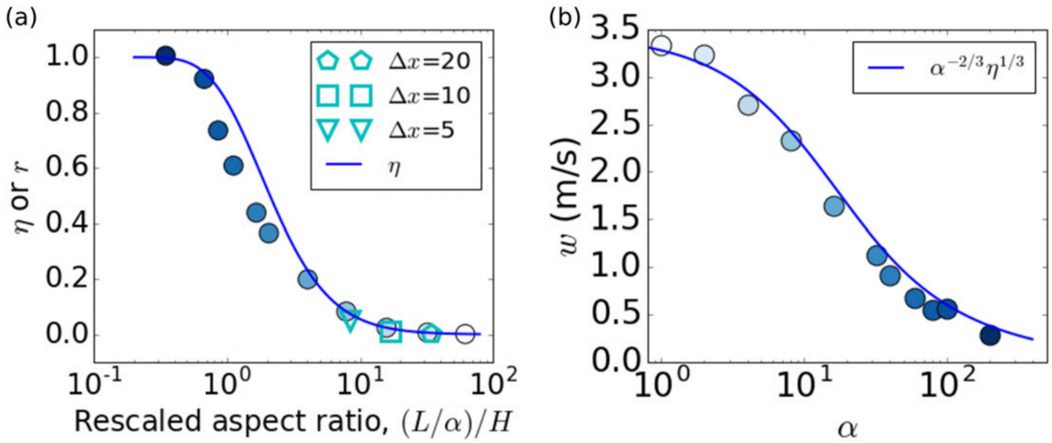

FIG. 9. (a) The theoretical η (curve) and measured nonhydrostasy ratios r (markers) for different Δx (marker shape) and α (marker color), as a function of the rescaled aspect ratio, $(L/\alpha)/H$. The analytical formula of $\eta = \beta/B$ follows Eq. (10a) of Jeevanjee (2017). The dimensionless r is defined by Eq. (4) and is normalized by an empirically determined constant to compare with theory. (b) Convective vertical velocity as a function of α, compared with a theoretical curve derived in section 5b.

rescaling creates biases at the large scale if α is increased by too much. In this section, we begin by describing the theoretical scaling of convective vertical velocity with Δx_{eff}. We then trace the dynamical route by which convection influences the eddy heat and momentum transport and the zonal mean climate.

a. *Vertical velocity of hypohydrostatic convection*

Analytical theory describing the dependence of convective vertical velocity on Δx has been developed in the literature, and it can be extended to apply to hypohydrostatic convection. In this subsection, we give a physical interpretation of the theory and then compare it to model solutions.

When convection is not fully resolved, its aspect ratio and vertical velocity are sensitive to Δx. The mechanism by which aspect ratio influences vertical velocity can be traced to the difference between the effective buoyancy β and the Archimedean buoyancy B (Jeevanjee 2017, and references therein). The former is the vertical acceleration experienced by the parcel, and the latter is the density difference between the parcel and the environment. Several analytical formulas have been derived for β/B as a function of the aspect ratio of a convective parcel (e.g., Pauluis and Garner 2006; Jeevanjee 2017). They have the same qualitative behaviors: $\beta \approx B$ for narrow parcels, and $\beta \ll B$ for wide parcels, such as those limited by a coarse grid spacing. The theory gives the dependence of w on Δx assuming that $w^2 \propto \beta$, and that the parcel width varies as Δx.

To compare with the analytical formula, we focus on strong convection that satisfies the conditions for mathematical similarity (fast, narrow and nonhydrostatic), rather than at every grid point as in Pauluis et al. (2006) or Boos et al. (2016). We accomplish this by focusing on the convective cluster defined in section 4a. For each convective cluster, the following nondimensional ratio is measured:

$$r \equiv \frac{\alpha^2 w^2}{\int B\, dz}, \tag{4}$$

where w is evaluated as the maximum vertical velocity over the volume of the convective cell, and B is approximated by $(\theta_{\mathrm{conv}} - \theta_{\mathrm{env}})g/\theta_{\mathrm{env}}$. The use of the maximum w and the integral in the denominator eliminates the vertical dimension. The numerator is the square of the rescaled vertical velocity, which is proportional to β. The denominator is known as the cloud buoyancy integral, and for undilute clouds it measures CAPE (e.g., Singh and O'Gorman 2015).

The ratio r is averaged over the identified convective clusters for each simulation. It is plotted in Fig. 9a as a function of the aspect ratio rescaled according to Eq. (2a), namely $(L/\alpha)/H$, where L and H are the typical width and depth that are insensitive across simulations. The eleven circular markers correspond to the 11 α values, and on this horizontal axis, α increases toward the left. The measured ratio r is compared with the analytical formula in Fig. 9a. The trend suggests that better resolved convection is more nonhydrostatic (upper-left corner).

The trend of the measured r is well captured by the theory, up to an empirically determined constant reflecting the detailed convective dynamics, such as the

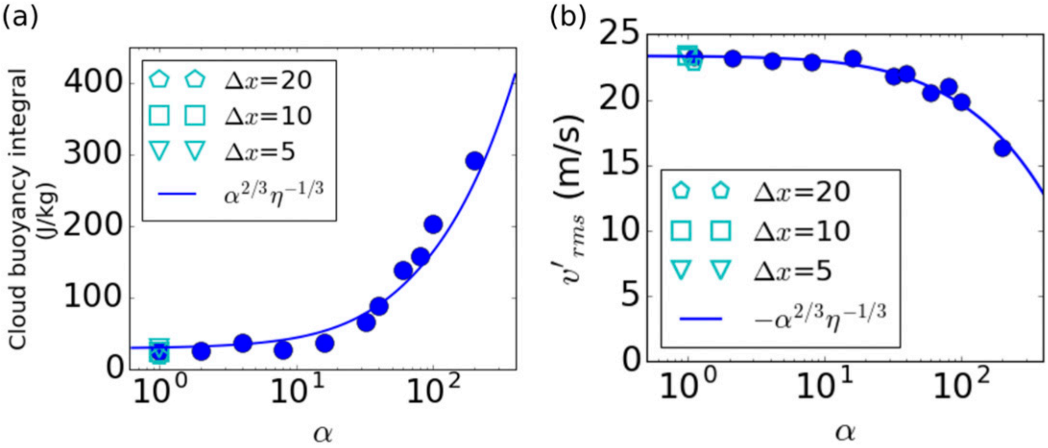

FIG. 10. (a) The cloud buoyancy integral in the warm sector and (b) v'_{rms} as functions of Δx and α.

drag coefficient and vertical profile of w. The theoretical ratio is denoted by $\eta \equiv \beta/B$, using Eq. (10a) of Jeevanjee (2017). The rapid change of r and η occurs between aspect ratios of 1 and 10, which characterizes the resolution gray zone. The agreement between the measured r and theoretical η, with the assumptions that $w^2 \propto \beta$ and that the parcel width is a constant multiple of Δx, supports the mechanisms described above. That is, the theory for β/B, and the grid-based similarity between the hypohydrostatic convection and its high-resolution counterpart, are verified.

Measurements from the high-resolution experiments with $\alpha = 1$ are also plotted in Fig. 9a as the polygonal markers at the bottom-right corner. The consistency with the α experiments is another piece of evidence for the similarity argument. The fact that they locate along the same analytical function η suggests that the hypohydrostatic rescaling correctly represents the resolution effect. Figure 9a suggests that convection at $\Delta x \geq 10$ km is approximately hydrostatic, where w doubles as Δx halves. The $\Delta x = 5$-km solution is barely inside the resolution gray zone and far from the convection-resolving limit in which w converges.

The next step is to analyze the dependence of w on α using the theory for η and r. Figure 9b shows w averaged over the identified convective cells for each α simulation. Note that in this horizontal axis, α increases toward the right, which is opposite to Fig. 9a. As expected, the vertical velocity decreases with α, which was already clear from the rain-rate snapshots (Fig. 5) and distributions (Fig. 7) discussed earlier. The decrease is monotonic but at nonuniform rates. The change is small from $\alpha = 1$ to 2 because the large aspect ratio (width over height) still renders the convection hydrostatic, and hydrostatic motions are insensitive to α. As α further increases, nonhydrostatic effects start to occur, so that the convective w decreases more quickly.

The theoretical curve in Fig. 9b combines the proportionality between r and η with an energy balance relation. Its analytical expression is $\alpha^{-2/3}\eta^{1/3}$, which will be derived in section 5b. The convective vertical velocity decreases by an order of magnitude as α increases from 1 to 200, which has important implications for the large-scale flow.

b. *Stratification in the warm sector of the eddy*

In this subsection, the stratification in the warm sector of the eddy is argued to be the connection between the decreasing convective activity and decreasing eddy intensity. The warm sector is defined as midlatitude regions having low-level $v > 0$ and precipitable water greater than 48 kg m^{-2}, corresponding to longitudes around 10°E in Fig. 4 where the low-level θ_e is much greater than the mean.

The cloud buoyancy integral is $\int B\,dz$, where $B = (\theta_{\mathrm{conv}} - \theta_{\mathrm{env}})g/\theta_{\mathrm{env}}$ as in section 5a. The environmental temperature θ_{env} is averaged over the warm sector. In Fig. 10a, each marker represents the average $\int B\,dz$ over all convective clusters in each simulation. They are indistinguishably small for $\alpha \lessapprox 16$, as well as for the high-resolution solutions. A small cloud buoyancy integral indicates a moist neutral warm sector. The convergence with resolution suggests that the 40-km convection is as efficient at maintaining moist neutrality as the better-resolved convection.

To explain the increase of cloud buoyancy integral for $\alpha \gtrapprox 16$, an analytical scaling is derived. Recall that Fig. 9a confirms the relation

$$\frac{\alpha^2 w^2}{\int B\,dz} \sim \eta\left(\frac{L/\alpha}{H}\right), \tag{5}$$

where η is an analytical formula as a function of the aspect ratio given by Eq. (10a) of Jeevanjee (2017). The η function interpolates between 1 in the $L/\alpha \ll H$ limit and $(\alpha H/L)^2$ times a constant in the $L/\alpha \gg H$ limit. To close the theory, a separate relation between w and $\int B\,dz$ is proposed as follows. Consider the generation and destruction rates of the cloud buoyancy integral in the warm sector. The generation is caused by radiative cooling and meridional heat fluxes, and the destruction is caused by convective overturning. Over its lifetime, convection adjusts the vertical temperature profile such that the cloud buoyancy integral is reduced to essentially zero. The time scale of convective overturning can be estimated by $H/(\sigma w)$, where H is the depth and σ is the temporal and spatial frequency of convection. Thus, the steady state balance between the generation and destruction rates can be expressed as

$$G \approx \frac{\int B\,dz}{H/(\sigma w)}, \tag{6}$$

where G denotes the generation rate of cloud buoyancy integral. Note that Eq. (6) is a scaling relation rather than an equality, where the variables are represented by the characteristic scales.

Eliminating w between Eqs. (5) and (6) gives the dependence of cloud buoyancy integral on α:

$$\int B\,dz \sim \frac{\alpha^{2/3}}{\eta[(L/\alpha)/H]^{1/3}}. \tag{7}$$

The cloud buoyancy integral has been normalized by $(GH/\sigma)^{3/2}$, which is assumed to be constant. This is reasonable because w and $\int B\,dz$, being directly related to convection, are the most sensitive terms to α in Eq. (6). Note that the function η is the same across experiments, but its argument depends on α. Similarly, Eq. (5) and Eq. (6) are combined to eliminate $\int B\,dz$, giving the theoretical w in Fig. 9b and matches data well.

The agreement between Eq. (7) and measured data in Fig. 10a helps interpret the nonuniform dependence on α. In the small aspect ratio (width over height) limit, either with small α or Δx, $\eta \rightarrow 1$ and $\int B\,dz$ approaches a small constant. That is, the 40-km convection is as efficient at maintaining a small cloud buoyancy integral as the 5-km convection. Small values of α are not able to modify the 40-km convection. But when α is large enough to do so, it slows the convection down to allow $\int B\,dz$ to build up. Even though the warm sector becomes more statically unstable, convection is inefficient at consuming the available buoyancy.

c. *Eddy intensity and transport*

Figure 10b shows that the eddy intensity decreases with α, which turns out to be negatively proportional to the cloud buoyancy integral in the warm sector. The markers represent the root-mean-square v', averaged over time around the latitude where it maximizes. The theoretical curve is simply Eq. (7) multiplied by a negative constant plus a constant shift. The reason for the negative proportionality between v'_{rms} and $\int B\,dz$ can be understood as follows.

Consider the free-tropospheric temperatures in the warm sector, cold sector, and convective clusters, denoted by θ_{warm}, θ_{cold}, and θ_{conv}, respectively. Under the anelastic approximation,

$$\int B\,dz \approx \frac{\theta_{\mathrm{conv}} - \theta_{\mathrm{warm}}}{\theta_0} gH, \tag{8}$$

where θ_0 is a reference potential temperature and H is a typical cloud depth. On the other hand, θ_{cold} is involved in the thermal wind balance that relates v'_{rms} to the temperature difference across the warm and cold sectors, which is mostly along the zonal direction:

$$f_0 \frac{v'_{\mathrm{rms}}}{H} \approx \frac{(\theta_{\mathrm{warm}} - \theta_{\mathrm{cold}})/\theta_0}{l} g, \tag{9}$$

where l is the zonal distance between the warm and cold sectors. Here v'_{rms} has been assumed to be dominated by the baroclinic component. Combining Eqs. (8) and (9),

$$\frac{\Delta v'_{\mathrm{rms}}}{\Delta \int B\,dz} \approx \frac{\Delta(\theta_{\mathrm{warm}} - \theta_{\mathrm{cold}})}{\Delta(\theta_{\mathrm{conv}} - \theta_{\mathrm{warm}})} \frac{1}{f_0 l} \approx -\frac{1}{f_0 l}, \tag{10}$$

where Δ denotes the difference between α experiments. The reasoning behind the second approximation, namely, $\Delta\theta_{\mathrm{cold}} \approx 0$ and $\Delta\theta_{\mathrm{conv}} \approx 0$, is as follows.

Among θ_{warm}, θ_{cold}, and θ_{conv}, the first temperature is the most sensitive to α. The sensitivity of θ_{conv}, which inherits the boundary layer properties, is limited by the fixed SST. That is, the increase of $\int B\,dz$ is caused by a colder θ_{warm} and a relatively constant θ_{conv}. The lack of deep convection in the cold sector makes θ_{cold} insensitive to α. Therefore, the ratio in Eq. (10) reduces to $-1/(f_0 l)$. Substituting in the reasonable values of $f_0 = 1.0 \times 10^{-4}\,\mathrm{s}^{-1}$ and $l = 500\,\mathrm{km}$, the proportionality constant works out to be $-2\,\mathrm{m\,s^{-1}}\,(100\,\mathrm{J\,kg^{-1}})^{-1}$. This simple estimate gives the order of magnitude of the measured value, $-2.2\,\mathrm{m\,s^{-1}}\,(100\,\mathrm{J\,kg^{-1}})^{-1}$, obtained by a linear regression between v'_{rms} and $\int B\,dz$ across α experiments.

In summary, the chain of reasoning from Eq. (5) to Eq. (10) suggests that very large α leads to slower convection, a colder warm sector, and hence a weaker

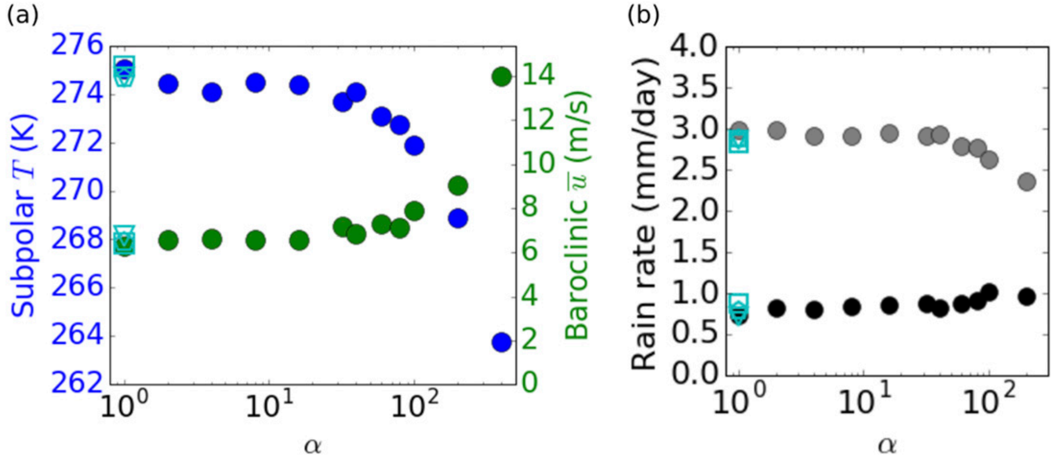

FIG. 11. (a) Mean temperature in the subpolar lower troposphere and the baroclinic component of $\overline{u}$ as functions of Δx and α. (b) Average rain rate as functions of Δx and α. The latitude of 33°N is chosen to separate the low latitudes (black) and midlatitudes (gray). The values are normalized by the respective area, so that the sum over latitudes represents the domain-mean rain rate.

eddy. The eddy intensity is insensitive to small α and Δx for the same reason that the cloud buoyancy integral is insensitive. These quantities have converged with resolution because the warm sector has reached moist neutrality. However, for very large α, this limit is not reached, and the resulting weakening of v'_{rms} is deemed a detrimental consequence.

As a consistency check, Figs. 9b and 10a show that w and $\int B\,dz$ both change by tenfold as α increases from 1 to 200. In the same range, v'_{rms} changes by only 30% in Fig. 10b, so it is reasonable to assume the large-scale variables to be constant when deriving the scaling relations. We have verified that the warm-sector cloud frequency σ and in-cloud temperature θ_{conv} remain constant despite the fact that they are related to convective and boundary layer processes. Presumably, this is because convection is confined to the warm sector by the baroclinic wave in this system, but this insensitivity may not be true for tropical convection.

The weakening of the eddy with very large α leads to a series of undesirable consequences on the mean climate. The poleward heat transport is reduced, which is balanced by a reduced longwave cooling in the subpolar latitudes. This is reflected in the subpolar cooling in Fig. 11a. By thermal wind balance, the zonal jet strengthens with α while the eddy weakens.

The reduction of cooling rate in the subpolar region influences the global energy balance. With larger α, the smaller cooling rate is balanced by a smaller rain rate. The reduction of rain rate occurs mainly in midlatitudes (Fig. 11b), consistent with the slowdown of convection and decrease of vertical moisture flux in the warm sector. Similar to the dependence of v'_{rms}, the domain-mean rain rate is independent of resolution and small α but decreases with very large α. This correlation between cyclone intensity and cyclone-wide precipitation is consistent with the observational study of Field and Wood (2007). The rain rate does not change much in the tropics, possibly because the tropics have a larger area in which convection is allowed to occur, so the frequency of convection can adjust to maintain the mean rain rate.

6. Conclusions and implications

We have combined a model-resolution study of explicit convection in a quasi-steady baroclinic eddy with an evaluation of the hypohydrostatic rescaling, which changes the effective resolution on a fixed grid. The quasi-steady eddy proves to be a useful system in which to study the convection–eddy interaction. Analyzing the statistically steady state avoids the complication of exploring the large phase space of initial conditions. After a couple weeks of spinup, the cyclone remains quasi steady for the 3-month duration of the experiment. It has all the features of a realistic mature cyclone, including a frontal squall line, comma cloud, and a low-level jet. As opposed to a developing eddy, where baroclinic instability intensifies the eddy by extracting available potential energy from the mean flow, moist convection is crucial in maintaining the intensity of the large-scale circulation in this stage.

The stratification in the warm sector is identified to be the pathway by which convection influences the eddy. A relation based on the balance of convective updraft [Eq. (5)], and the balance between the generation and destruction rates of the cloud buoyancy integral [Eq. (6)], has been derived. Combined with thermal wind balance for the vertical shear of v, the relation explains the weakening of the eddy with very large α, as well as the insensitivity to Δx for fixed α. In essence, convection at $\Delta x = 40$ km, whose typical overturning time is less than an hour, is as efficient at maintaining the moist neutrality as that at $\Delta x = 5$ km. This convergence with resolution is consistent with Booth et al. (2013), where the peak intensity of a baroclinic life cycle is indistinguishable in simulations with $\Delta x = 50$ to 25 km.

The undesirable weakening of the eddy becomes statistically significant when $\alpha \gtrapprox 16$ with $\Delta x = 40$ km. It is accompanied by a decrease in moist static energy transport, which is associated with a weakened global energy throughput and a strengthened jet. The mean climate becomes substantially different from the high-resolution simulations, suggesting that very large α should be avoided.

When $\alpha \lessapprox 16$, the large-scale flow is insensitive to α because the rescaling effect is constrained by the grid spacing. This is consistent with the evaluation of Singh and Kuang (2016), who found that $\alpha = 10$ at 40 km produced the same climate as $\alpha = 1$ on a narrow equatorial β plane.

In the regime of low impact on the large scale, the hypohydrostatic rescaling may be useful for improving some convective-scale properties. This model has no significant resolution error in eddy intensity, but as α increases the distribution of rain rate better matches the high-resolution solution, and the individual convective cells are better resolved. Both effects are consistent with the similarity argument based on the effective resolution. If the quantity of interest is related to those effects, such moderate values of α may provide benefits while not introducing errors in the large-scale flow. The positive results by the rescaling in improving the TC intensity in Boos et al. (2016) and Fedorov et al. (2018) may lie in this regime.

When applied to a convection-permitting grid, the hypohydrostatic rescaling has the potential of making the effective grid spacing convection resolving without undesirable biases in the large scale. Equation (7) can be used to estimate an upper bound of useful α for a given Δx, if the background stratification is set by buoyant convection. For example, for a high-resolution GCM having a 25-km grid spacing, suppose that at $\alpha = 1$ the cloud buoyancy integral is close to zero. If our tolerable limit for the increased cloud buoyancy integral at larger α is taken to be triple the value at $\alpha = 1$, Eq. (7) gives $\alpha < 2.5$. Values of $L = 4\Delta x$ and $H = 10$ km typical for deep convection have been used. The largest tolerable α has a corresponding $\Delta x_{\text{eff}} = 10$ km, which is still in the resolution gray zone. On the other hand, suppose that in a new cloud-permitting experiment the model grid spacing is 5 km. The largest tolerable α is 5.2, corresponding to $\Delta x_{\text{eff}} = 0.96$ km. In this case, the strong convection is expected to be better resolved. Better resolved convection is less sensitive to model details, such as grid structure or hyperdiffusion, which may allow a more physically meaningful solution.

Independent of the hypohydrostatic scaling, this model of a quasi-steady eddy, having a well-defined amplitude and phase speed, provides a clean test bed for theories of moist baroclinic eddies and associated physical processes. For instance, a quasi-steady-state moisture budget within a baroclinic cyclone is used to explain midlatitude cloud feedback in McCoy et al. (2019). This setup cleanly isolates the eddy, avoiding complications due to climate variability in a global model.

Acknowledgments. We thank Olivier Pauluis, Nadir Jeevanjee, Xi Chen, and Zhiming Kuang for discussion and feedback on earlier versions of this manuscript. This report was prepared by Tsung-Lin Hsieh under Award NA18OAR4320123 from the National Oceanic and Atmospheric Administration, U.S. Department of Commerce. The statements, findings, conclusions, and recommendations are those of the author(s) and do not necessarily reflect the views of the National Oceanic and Atmospheric Administration, or the U.S. Department of Commerce. Data used in this research are archived at the Geophysical Fluid Dynamics Laboratory and are available upon request.

REFERENCES

Anderson, J. L., and Coauthors, 2004: The new GFDL global atmosphere and land model AM2–LM2: Evaluation with prescribed SST simulations. *J. Climate*, **17**, 4641–4673, https://doi.org/10.1175/JCLI-3223.1.

Boos, W. R., and Z. Kuang, 2010: Mechanisms of poleward propagating, intraseasonal convective anomalies in cloud system–resolving models. *J. Atmos. Sci.*, **67**, 3673–3691, https://doi.org/10.1175/2010JAS3515.1.

——, A. Fedorov, and L. Muir, 2016: Convective self-aggregation and tropical cyclogenesis under the hypohydrostatic rescaling. *J. Atmos. Sci.*, **73**, 525–544, https://doi.org/10.1175/JAS-D-15-0049.1.

Booth, J. F., S. Wang, and L. Polvani, 2013: Midlatitude storms in a moister world: Lessons from idealized baroclinic life cycle experiments. *Climate Dyn.*, **41**, 787–802, https://doi.org/10.1007/s00382-012-1472-3.

——, C. M. Naud, and J. Willison, 2017: Evaluation of extratropical cyclone precipitation in the North Atlantic basin: An analysis of ERA-Interim, WRF, and two CMIP5 models. *J. Climate*, **31**, 2345–2360, https://doi.org/10.1175/JCLI-D-17-0308.1.

Boutle, I. A., S. E. Belcher, and R. S. Plant, 2011: Moisture transport in midlatitude cyclones. *Quart. J. Roy. Meteor. Soc.*, **137**, 360–373, https://doi.org/10.1002/qj.783.

Bretherton, C. S., 2007: Challenges in numerical modeling of tropical circulations. *The Global Circulation of the Atmosphere*,

T. Schneider and A. H. Sobel, Eds., Princeton University Press, 302–330.

Fedorov, A. V., L. Muir, W. R. Boos, and J. Studholme, 2018: Tropical cyclogenesis in warm climates simulated by a cloud-system resolving model. *Climate Dyn.*, **52**, 107–127, https://doi.org/10.1007/s00382-018-4134-2.

Field, P. R., and R. Wood, 2007: Precipitation and cloud structure in midlatitude cyclones. *J. Climate*, **20**, 233–254, https://doi.org/10.1175/JCLI3998.1.

Garner, S. T., D. M. W. Frierson, I. M. Held, O. Pauluis, and G. K. Vallis, 2007: Resolving convection in a global hypohydrostatic model. *J. Atmos. Sci.*, **64**, 2061–2075, https://doi.org/10.1175/JAS3929.1.

Grenier, H., and C. S. Bretherton, 2001: A moist PBL parameterization for large-scale models and its application to subtropical cloud-topped marine boundary layers. *Mon. Wea. Rev.*, **129**, 357–377, https://doi.org/10.1175/1520-0493(2001)129<0357:AMPPFL>2.0.CO;2.

Jeevanjee, N., 2017: Vertical velocity in the gray zone. *J. Adv. Model. Earth Syst.*, **9**, 2304–2316, https://doi.org/10.1002/2017MS001059.

Knutson, T. R., J. J. Sirutis, S. T. Garner, I. M. Held, and R. E. Tuleya, 2007: Simulation of the recent multidecadal increase of Atlantic hurricane activity using an 18-km-grid regional model. *Bull. Amer. Meteor. Soc.*, **88**, 1549–1565, https://doi.org/10.1175/BAMS-88-10-1549.

——, and Coauthors, 2013: Dynamical downscaling projections of twenty-first-century Atlantic hurricane activity: CMIP3 and CMIP5 model-based scenarios. *J. Climate*, **26**, 6591–6617, https://doi.org/10.1175/JCLI-D-12-00539.1.

Krueger, S. K., Q. Fu, K. N. Liou, and H.-N. S. Chin, 1995: Improvements of an ice-phase microphysics parameterization for use in numerical simulations of tropical convection. *J. Appl. Meteor.*, **34**, 281–287, https://doi.org/10.1175/1520-0450-34.1.281.

Kuang, Z., P. N. Blossey, and C. S. Bretherton, 2005: A new approach for 3D cloud-resolving simulations of large-scale atmospheric circulation. *Geophys. Res. Lett.*, **32**, L02809, https://doi.org/10.1029/2004GL021024.

Lackmann, G. M., 2002: Cold-frontal potential vorticity maxima, the low-level jet, and moisture transport in extratropical cyclones. *Mon. Wea. Rev.*, **130**, 59–74, https://doi.org/10.1175/1520-0493(2002)130<0059:CFPVMT>2.0.CO;2.

Lebo, Z. J., and H. Morrison, 2015: Effects of horizontal and vertical grid spacing on mixing in simulated squall lines and implications for convective strength and structure. *Mon. Wea. Rev.*, **143**, 4355–4375, https://doi.org/10.1175/MWR-D-15-0154.1.

Ma, D., W. Boos, and Z. Kuang, 2014: Effects of orography and surface heat fluxes on the South Asian summer monsoon. *J. Climate*, **27**, 6647–6659, https://doi.org/10.1175/JCLI-D-14-00138.1.

——, A. H. Sobel, Z. Kuang, M. S. Singh, and J. Nie, 2019: A moist entropy budget view of the South Asian summer monsoon onset. *Geophys. Res. Lett.*, **46**, 4476–4484, https://doi.org/10.1029/2019GL082089.

McCoy, D. T., and Coauthors, 2019: Cloud feedbacks in extratropical cyclones: Insight from long-term satellite data and high-resolution global simulations. *Atmos. Chem. Phys.*, **19**, 1147–1172, https://doi.org/10.5194/acp-19-1147-2019.

Oertel, A., M. Boettcher, H. Joos, M. Sprenger, H. Konow, M. Hagen, and H. Wernli, 2019: Convective activity in an extratropical cyclone and its warm conveyor belt—A case-study combining observations and a convection-permitting model simulation. *Quart. J. Roy. Meteor. Soc.*, **145**, 1406–1426, https://doi.org/10.1002/qj.3500.

Orlanski, I., 2003: Bifurcation in eddy life cycles: Implications for storm track variability. *J. Atmos. Sci.*, **60**, 993–1023, https://doi.org/10.1175/1520-0469(2003)60<993:BIELCI>2.0.CO;2.

Pauluis, O., and S. Garner, 2006: Sensitivity of radiative–convective equilibrium simulations to horizontal resolution. *J. Atmos. Sci.*, **63**, 1910–1923, https://doi.org/10.1175/JAS3705.1.

——, D. M. W. Frierson, S. T. Garner, I. M. Held, and G. K. Vallis, 2006: The hypohydrostatic rescaling and its impacts on modeling of atmospheric convection. *Theor. Comput. Fluid Dyn.*, **20**, 485–499, https://doi.org/10.1007/s00162-006-0026-x.

Peters, M. E., and C. S. Bretherton, 2006: Structure of tropical variability from a vertical mode perspective. *Theor. Comput. Fluid Dyn.*, **20**, 501–524, https://doi.org/10.1007/s00162-006-0034-x.

Semane, N., and P. Bechtold, 2015: Convection and waves on small Earth and deep atmosphere. *Tellus*, **67A**, 25151, https://doi.org/10.21957/ZOGU3GJ50.

Singh, M. S., and P. A. O'Gorman, 2015: Increases in moist-convective updraught velocities with warming in radiative-convective equilibrium. *Quart. J. Roy. Meteor. Soc.*, **141**, 2828–2838, https://doi.org/10.1002/qj.2567.

——, and Z. Kuang, 2016: Exploring the role of eddy momentum fluxes in determining the characteristics of the equinoctial Hadley circulation: Fixed-SST simulations. *J. Atmos. Sci.*, **73**, 2427–2444, https://doi.org/10.1175/JAS-D-15-0212.1.

——, ——, and Y. Tian, 2017: Eddy influences on the strength of the Hadley circulation: Dynamic and thermodynamic perspectives. *J. Atmos. Sci.*, **74**, 467–486, https://doi.org/10.1175/JAS-D-16-0238.1.

Thorncroft, C. D., B. J. Hoskins, and M. E. McIntyre, 1993: Two paradigms of baroclinic-wave life-cycle behaviour. *Quart. J. Roy. Meteor. Soc.*, **119**, 17–55, https://doi.org/10.1002/qj.49711950903.

Willison, J., W. A. Robinson, and G. M. Lackmann, 2013: The importance of resolving mesoscale latent heating in the North Atlantic storm track. *J. Atmos. Sci.*, **70**, 2234–2250, https://doi.org/10.1175/JAS-D-12-0226.1.

Wu, L., and Coauthors, 2014: Simulations of the present and late-twenty-first-century western North Pacific tropical cyclone activity using a regional model. *J. Climate*, **27**, 3405–3424, https://doi.org/10.1175/JCLI-D-12-00830.1.